Chemical Science

ROYAL SOCIETY OF CHEMISTRY

EDGE ARTICLE

View Article Online
View Journal | View Issue

Check for updates

Cite this: *Chem. Sci.*, 2021, **12**, 5236

All publication charges for this article have been paid for by the Royal Society of Chemistry

Received 22nd January 2021
Accepted 19th February 2021

DOI: 10.1039/d1sc00416f

rsc.li/chemical-science

Tuning energy landscapes and metal–metal interactions in supramolecular polymers regulated by coordination geometry†

Nils Bäumer,[a] Kalathil K. Kartha,[a] Stefan Buss,[b] Iván Maisuls,[b] Jasnamol P. Palakkal,[c] Cristian A. Strassert[b] and Gustavo Fernández *[a]

Herein, we exploit coordination geometry as a new tool to regulate the non-covalent interactions, photophysical properties and energy landscape of supramolecular polymers. To this end, we have designed two self-assembled Pt(II) complexes **1** and **2** that feature an identical aromatic surface, but differ in the coordination and molecular geometry (linear *vs.* V-shaped) as a result of judicious ligand choice (monodentate pyridine *vs.* bidentate bipyridine). Even though both complexes form cooperative supramolecular polymers in methylcyclohexane, their supramolecular and photophysical behaviour differ significantly: while the high preorganization of the bipyridine-based complex **1** enables an H-type 1D stacking with short Pt···Pt contacts *via* a two-step consecutive process, the existence of increased steric effects for the pyridyl-based derivative **2** hinders the formation of metal–metal contacts and induces a single aggregation process into large bundles of fibers. Ultimately, this fine control of Pt···Pt distances leads to tuneable luminescence—red for **1** *vs.* blue for **2**, which highlights the relevance of coordination geometry for the development of functional supramolecular materials.

Introduction

Self-assembled nanomaterials have emerged in the past decades as potential candidates for various applications.[1–5] Fueled by the desire to control the pathways[6–9] and the resulting functional properties[10–12] of such supramolecular assemblies, detailed structure–property relationships have been successfully established,[13,14] with particular focus on organic compounds.[15–17] In recent years, molecular design strategies[18,19] have been successfully exploited to drive and control molecular self-assembly processes.[20–22] The intriguing possibilities that arise from adding metal ions into the mix[23–26] have kickstarted the relatively young field of metal-based supramolecular polymers.[26] Due to the wide variety of available ligands and metal ions capable of forming supramolecular polymers, the structural diversity of such compounds is immense.[27–31] Consequently, metal complexes have been investigated as supramolecular building blocks in a highly diverse manner for manifold applications.[32–34] However, these miscellaneous studies render a structure-based optimization of these systems challenging. For example, geometrical modifications are often accompanied by additional structural differences, such as inclusion or variation of linkers, solubilizing chains or coordinating atoms.[35–38] Further, electronic effects are rarely discussed and can be difficult to predict.[39,40] Particularly, in contrast to discrete supramolecular systems such as helicates,[41,42] catenanes[43,44] or cages,[45,46] the coordination geometry is often underappreciated in the context of metallosupramolecular polymerization. While there are countless studies utilizing mono-,[47–49] bi-,[50–52] and tridentate[53–55] ligands, the effect of changing the ligand system is typically excluded from discussion and often consequential differences in molecular design render such comparisons unfeasible. Moreover, a simple coordination geometry change (*cis*-/*trans*-isomerism) is difficult to investigate due to the rapid interconversion between both species in solution.[56,57]

Mono- and polydentate ligands in complexes of d^8 transition metals based on N-heterocyclic aromatics have attracted considerable attention in supramolecular chemistry.[58] Owing to their preorganized square-planar geometry favoring stacking,[59,60] they are prone to undergo supramolecular polymerization, gaining further stabilization by metal–metal and/or hydrogen bonding interactions.[61,62] In addition, the intriguing photophysical properties of these molecules provide access to various applications, such as in optoelectronics or sensing.[63–65]

[a]*Organisch-Chemisches Institut, Westfälische Wilhelms-Universität Münster, Corrensstraße 36, 48149 Münster, Germany. E-mail: fernandg@uni-muenster.de*
[b]*CeNTech, CiMIC, SoN, Institut für Anorganische und Analytische Chemie, Westfälische Wilhelms-Universität Münster, Heisenbergstraße 11, 48149, Germany*
[c]*Technische Universität Darmstadt, Department of Materials and Earth Sciences, Alarich-Weiss-Straße 2, 64287 Darmstadt, Germany*

† Electronic supplementary information (ESI) available: Experimental section, synthetic details, complete spectroscopic characterization, variable temperature/solvent UV-Vis studies, ^{1}H NMR studies, photoluminescence studies, AFM imaging, phosphorescence lifetime measurements, XRD diffraction. See DOI: 10.1039/d1sc00416f

However, while many studies have focused on modifying ligands to create diverse binding motifs or differences in sterics, there is a distinct lack of structure–property relationships in terms of coordination geometry changes.

To bridge this knowledge gap, we have herein designed and synthesized Pt(II) complexes **1** and **2** (Scheme 1), which feature a similar ligand design but differ in the coordination geometry (bidentate V-shaped "*cis*" **1** *vs.* monodentate linear "*trans*" **2**). This structural modification greatly influences the molecular preorganization of the system, enabling the establishment of distinct non-covalent interactions, which in turn dictate the photophysical properties and the energy landscapes of the systems. While the molecular geometry for **1** enforces short Pt···Pt contacts driven by an efficient overlap of the aromatic oligophenyleneethynylene (OPE) ligands, the out-of-plane arrangement of the Cl ligands at the Pt(II) center for **2** hinders the formation of short Pt···Pt contacts by precluding a parallel molecular packing, leading to a minor translational offset. Ultimately, the distinct interplay of interactions for **1** and **2** leads to significant differences in luminescence and energy landscapes – two-step *vs.* single-step self-assembly for **1** and **2**, respectively. Detailed investigation of these complexes allowed us to unravel for the first time how changes in the coordination geometry affect supramolecular polymerization.

Results and discussion

Photophysical analysis

Initially, we probed the self-assembly of **1** and **2** by solvent-dependent UV/Vis studies (Fig. 1a and d). Complex **1** exhibits two high-energy absorption bands in all investigated solvents (around 310 and 330 nm in MCH, *n*-hexane, chloroform and DCM; and at 310 and 349 nm in THF). These bands can be readily assigned to intraligand (IL) transitions into excited states with π–π* as well as n–π* character.[66] Furthermore, two additional high-energy absorption bands (around 349 and 373 nm) can also be observed in solvents of slightly higher polarity (DCM and chloroform). In low-polarity solvents (MCH and *n*-hexane), these bands only appear as shoulders. Additionally, one low-energy absorption band (423 and 429 nm in DCM and chloroform, respectively) can be observed in higher polarity solvents and two low-energy absorption bands (404 and 428 nm) in apolar solvents (MCH and *n*-hexane). Based on the strong solvatochromic effect in the low energy region of the UV/Vis spectrum, we assign these bands to transitions into metal-to-ligand charge-transfer (MLCT) states.[67] Moreover, a minor contribution of ligand-to-ligand charge-transfer (LLCT) character involving the halogen and bipyridine ligands is also expected, as previously reported for this spectral region.[68] On this basis, we conclude that non-polar solvents (such as MCH or *n*-hexane) induce aggregation, whereas more polar solvents (such as chloroform) favor the molecularly dissolved state.[69] On the other hand, solvent-dependent UV/Vis studies of **2** reveal a similar aggregation propensity in non-polar media, although differences are also appreciable (Fig. 1d). In particular, the spectra in most solvents at low concentration (10^{-5} M) are almost identical, showing an absorption maximum at ~350 nm and a shoulder around 370 nm. These spectral signatures can be assigned to transitions into metal perturbed IL (main peak) as well as MLCT states (shoulder).[70,71] The only exception is the spectrum in *n*-hexane, where a double band at 353 and 365 nm with an additional absorption maximum at 401 nm are noticed. Additionally, a significant hypochromism compared to all other solvents can be observed, which is concomitant with the increase in optical density in the low energy region (>400 nm). An identical trend is observed for solutions in MCH at slightly higher concentrations (3×10^{-5} M). Consequently, we identified solvents of high polarity (such as chloroform) as good solvents, while low polarity solvents (such as MCH and *n*-hexane) can be considered as poor solvents suitable for aggregation studies.

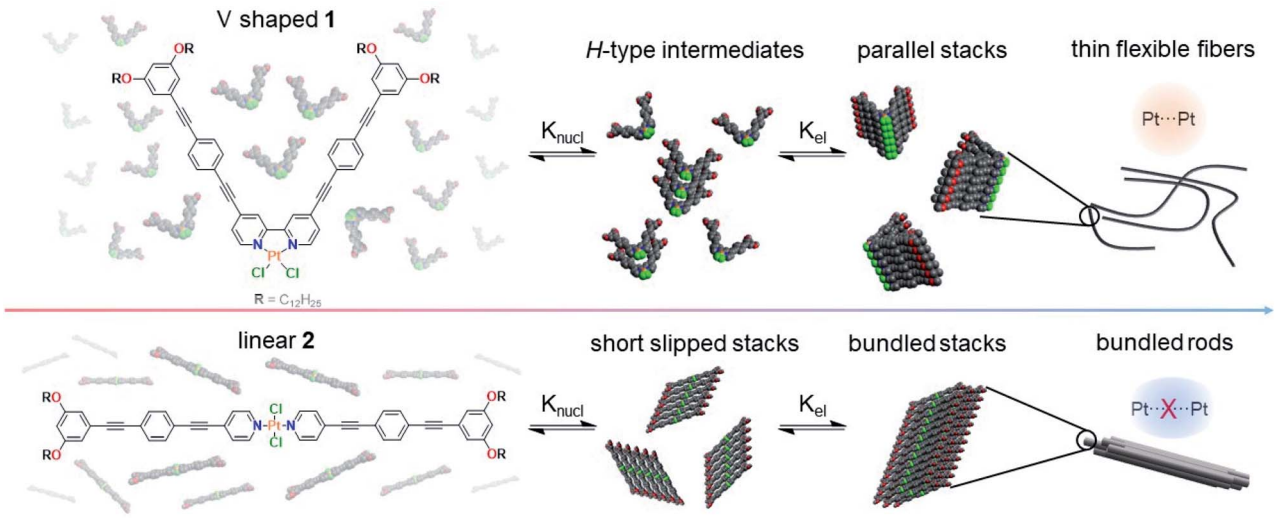

Scheme 1 Chemical structures of Pt(II) complexes **1** and **2** and cartoon representation of their supramolecular polymerization in MCH leading to different emission properties induced by close (top, orange) or weak Pt···Pt contacts (bottom, blue). Alkyl chains have been reduced to methyl groups for better visibility.

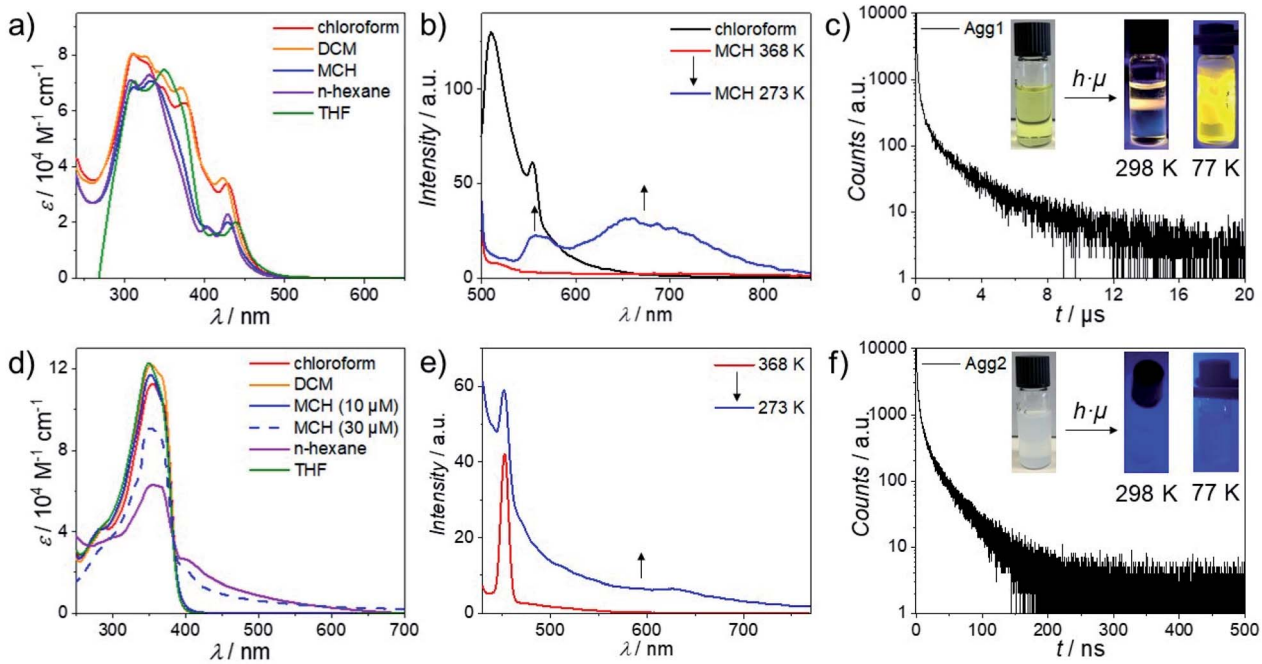

Fig. 1 Solvent-dependent UV/Vis spectra of **1** (a) and **2** (d) at 10^{-5} M and 298 K; VT-photoluminescence spectra of **1** (b) and **2** (e) at 3×10^{-6} M (b) and 30×10^{-6} M (e); cooling rate: 1 K min^{-1}. The photoluminescence spectrum of **1** in chloroform at 298 K has been added for reference; time-resolved photoluminescence decay of **Agg1** (c) and **Agg2** (f) in deaerated MCH at 298 K and 10^{-5} M, including the residuals ($\lambda_{exc} = 376.7$ nm, $\lambda_{em} = 690$ nm for **Agg1**; $\lambda_{exc} = 376.7$ nm, $\lambda_{em} = 550$ nm for **Agg2**). Inset: photographs of the used solutions at ambient conditions and under UV light ($\lambda_{exc} = 405$ nm) at 298 K and 77 K, respectively.

Subsequently, we performed variable temperature (VT)-photoluminescence studies of **1** in MCH between 368 K and 273 K (Fig. 1b and S13†). During initial cooling, only minor changes in the emission were observed; however, below 350 K, a broad emission between 600 and 850 nm showed up, a behavior that has been typically attributed to a ^{3}MMLCT state for structurally related compounds.[72] In addition, **1** showed a featureless emission band at 560 nm at lower temperature (<308 K), which can be assigned to ^{1}(d,π)–π* excited states.[73]

To further probe the existence of metal–metal interactions, we performed additional photoluminescence measurements. Initially, the emission spectra of **1** in a molecularly dissolved state (in chloroform) and in an aggregated form (in MCH) were compared to confirm whether the observed emission is caused by aggregation, or by a subsequent decrease in molecular rotation during cooling (Fig. 1b). To our satisfaction, no emission at low energies was observed in chloroform, confirming that aggregation-induced emission takes place. In order to assign these emission bands, we turned to phosphorescence lifetime measurements. To this end, we prepared **Agg1** by cooling a hot monomer solution (1×10^{-5} M) of **1** in MCH from 368 K to 298 K at a rate of 1 K min^{-1}. Afterwards, the solution was deaerated by purging with argon (Fig. 1c and S14–S20†). The excited state of **Agg1** shows a relatively long average lifetime of 0.67 μs (amplitude weighted). Cooling the aggregate solution to 77 K extends the long lifetimes to 20.6 μs. Interestingly, Gray and co-workers were able to correlate a linear relationship between the emission maximum from the ^{3}MMLCT state to the inverse cube of the Pt···Pt distance for a structurally related compound Pt(bpy)Cl$_2$.[74] Based on this linear relationship, the Pt···Pt distance in **Agg1** was estimated to be ~3.30 Å. Additionally, the emission at 560 nm observed at temperatures below 308 K can be assigned to an IL state, based on the relatively short average lifetime of 1.2 ns.

The self-assembly of **2** was also probed using VT-fluorescence spectroscopy revealing minor emission above 600 nm (Fig. 1e). Instead, a relatively sharp emission with a maximum at 380 nm typical for an IL ^{1}π–π* state accompanied by a vibronic structure can be observed (Fig. S21†). These findings can be attributed to stretching of the phenyl rings as well as the ethynylene units.[75–77]

Based on the results obtained from VT-luminescence, we envisage that the supramolecular packing of **2** can be described as a nearly parallel, short slipped aggregate with Pt···Pt distances (>4.0 Å) larger than the sum of van der Waals radii (3.5 Å),[78] as previously observed for related OPE-based bispyridyldichlorido Pt(II) complexes.[47] To validate this hypothesis, we conducted photoluminescence lifetime measurements (Fig. 1f and S21–S25†) using the free pyridyl ligand as reference compound (Fig. S26 and S27†). The average lifetime of the excited state of **Agg2** was only 9.7 ns, while for the free ligand a lifetime of 0.8 ns was obtained. Due to the comparable order of magnitude as well as the generally similar emission profile, the luminescence of the free ligand likely originates from the OPE system, while the emission of **Agg2** can be best described as originated by metal perturbed IL states, without any MMLCT contributions; here, the short lifetime is related to a fast radiationless deactivation promoted by thermally accessible low-

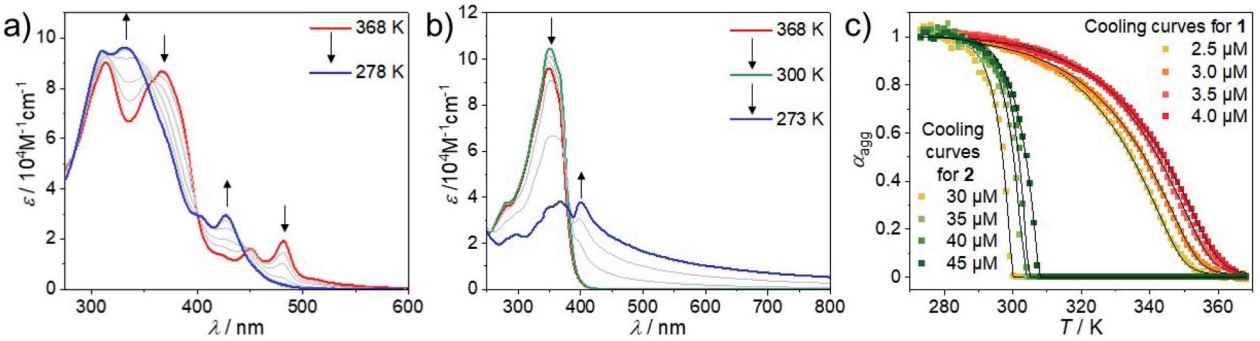

Fig. 2 VT-UV/Vis spectra of **1** (a) and **2** (b) between 368 K and 278 K or 273 K at 3×10^{-6} M (a) and 30×10^{-6} M (b); cooling rate: 1 K min^{-1}. (c) Plot of α_{agg} *vs.* T for **1** ($\lambda = 475$ nm) and **2** ($\lambda = 400$ nm) derived from cooling experiments and fitting to the nucleation–elongation model.[84]

lying metal centered (MC) states (d–d*) with dissociative character caused by the weak ligand field of the Cl ligands and the non-coplanar arrangement of the pyridine ligands.

From these results, we understand that in the case of **Agg1**, the MMLCT states act as energy traps from which the thermal population of such MC states is slowed down, which hampers non-radiative deactivation and leads to longer lifetimes. The out of plane torsional distortion of the pyridine ligands in **Agg2** probably hinders efficient Pt···Pt interactions, as previously observed in Pt(II) complexes with C^N^N luminophores and diverse ancillary ligands.[79]

Energy landscape elucidation

VT-UV/Vis studies in MCH (3×10^{-6} M) were initially conducted to gain a better understanding of the self-assembly behaviour of **1** (Fig. 2a and S28†). At 368 K, **1** shows two absorption bands at 450 nm and 475 nm, which can be attributed to the MLCT state of the molecularly dissolved state.[69] Cooling down to 278 K leads to a decrease of the maxima at 450 nm and 475 nm and a simultaneous increase of an absorption band at 430 nm, with an appreciable second absorption maximum at 404 nm. A similar hypsochromic shift of 4 and 35 nm is observed for the high energy absorption bands at 313 and 367 nm, respectively. This spectral pattern is in agreement with an H-type aggregation process.[80] In contrast to **1**, **2** requires significantly higher concentrations to aggregate in MCH solution (Fig. 2b, c and S30†). At high temperatures (>300 K), a minor hyperchromism with no isosbestic points can be observed, a phenomenon that has been previously assigned to the planarization of the aromatic surface.[81,82] Further cooling below a critical temperature (300 K) leads to a sudden drop in absorbance and a concurrent aggregate band formation at 400 nm that spreads up to *ca.* 700 nm (Fig. 2b). Additionally, the absorption maximum shows a bathochromic shift from 350 to 367 nm, indicating that the monomers of **2** are packed with a slight translational offset.[83] The increase in optical density in the low energy region above 450 nm indicates the formation of poorly solvated aggregates. Plotting the degree of aggregation (α_{agg}) of **1** *vs.* temperature (T) at 475 nm shows a steep, non-sigmoidal curve (Fig. 2c), indicating a cooperative supramolecular polymerization (Fig. 2c).[84] Similarly, a cooperative aggregation mechanism could be identified for **2** by plotting α_{agg} *vs.* T at 400 nm (Fig. 2c). These observations could be confirmed by denaturation studies, revealing poorly solvated aggregates that disassemble in a clearly non-sigmoidal fashion (Fig. S31†).

In comparison to **1**, the self-assembly of **2** shows a significantly more pronounced all-or-nothing behavior, which is reflected in the larger nucleation penalty of **2** (22.5 *vs.* 17.3 kJ mol^{-1}) in combination with a much larger elongation enthalpy (189 *vs.* 49 kJ mol^{-1}, respectively, Table 1). The smaller nucleation penalty of **1** can be rationalized by the molecular preorganization induced by the bipyridine binding site, which forces a planar coordination environment. In contrast, *trans*-oriented monodentate pyridine complexes are arranged out-of-plane, typically allowing both inter- and intramolecular hydrogen bonds between the halogens and the aromatic C–H groups from the pyridine moieties.[37,49] This potential steric hindrance during the initial nucleus formation is also reflected in the nucleation constant (K_n), which is one order of magnitude lower for **2** than it is for **1**. On the other hand, the elongation constant (K_e) remains within the same order of magnitude leading to a noticeably smaller cooperativity factor (1.2×10^{-4} *vs.* 27.1×10^{-4}) for **2**. This is a direct consequence of the change in coordination geometry, as the linear complex **2** can balance the steric demand and attractive intermolecular interactions, while a translational offset for **1** would not be feasible. Notably, careful investigation of the VT spectral changes of **1** reveals a transition between two species during

Table 1 Thermodynamic parameters derived from VT-UV/Vis experiments of **1** and **2** on the basis of the nucleation–elongation model using a global fitting[84]

	1	**2**
c [10^{-6} M]	3.0	30
ΔH_e [kJ mol^{-1}]	−48.9 ± 0.3	−189.1 ± 1.3
ΔH_n [kJ mol^{-1}]	−17.3 ± 0.2	−22.5 ± 1.9
ΔS° [kJ mol^{-1}]	−0.034 ± 0.001	−0.535 ± 0.004
ΔG° [kJ mol^{-1}]	−38.9 ± 0.4	−29.7 ± 1.8
T_e [K]	351.6 ± 0.1	299.9 ± 0.1
K_e [10^4 M^{-1}]	32.3	10.0
K_n [M^{-1}]	876	12
σ [10^{-4}]	27.1	1.2

cooling from 368 K to 313 K (Fig. 3a and b). Most likely, this transition corresponds to the aggregation of the monomer **Mon1** into an intermediate species **Int1**. In a second step, between 313 K and 283 K, a second transformation occurs, where **Int1** converts to the thermodynamic aggregate **Agg1** (Fig. 3a). Monitoring the absorption changes at 370 nm as well as the depletion of the monomer at 475 nm allows us to qualitatively estimate the relative concentration of all active species during the aggregation process (Fig. 3c and S32; see ESI† for methodology).[75] Time-dependent UV/Vis studies at variable concentrations (Fig. 3d, for full spectra see Fig. S33†) reveal that the transformation of **Int1** to **Agg1** is accelerated upon increasing concentration, indicating that **Int1** is an on-pathway intermediate towards **Agg1**.[85] The self-assembly of **1** follows a two-step dual cooperative process, as shown in the qualitative energy diagram depicted in Fig. 3e. Based on the small changes in UV/Vis during the second step, both **Int1** and **Agg1** can be identified as H-type aggregates with similar packing, where **Agg1** represents a more ordered structure. Additionally, given the rapid **Int1** → **Agg1** transformation and the fact that the monomer depletion does not seem to be influenced by the onset of elongation of **Agg1**, we assign **Int1** as an on-pathway transient species, possibly a dimer or short oligomer. In contrast, the self-assembly of **2** follows a one-step cooperative process with a higher activation energy compared to **1**, which is evident from the decrease in K_n as well as a sharp decrease in T_e.[86] The observation of pathway complexity only for compound **1** clearly reflects the noteworthy influence of coordination geometry on self-assembly. In fact, our results reveal that on-pathway intermediates can be stabilized by decreasing steric demands (in-plane arrangement of Cl ligands for **1** *vs.* out-of-plane arrangement for **2**). This behavior strongly differs from the majority of systems exhibiting off-pathway kinetic species,[85,87] where increased steric interactions stabilize the kinetic product.

Structural and morphological elucidation

Solvent- and temperature-dependent ^{1}H NMR studies were used to examine the supramolecular packing of **1**. Initially, we recorded a ^{1}H NMR spectrum of monomeric **1** in $CDCl_3$ at 1 mM and subsequently added increasing volume fractions of MCH-d_{14} to this solution. The stepwise addition of MCH-d_{14} leads to marked signal shifts accompanied by progressive broadening, suggesting a self-assembly process (Fig. 4a). Throughout the entire polarity spectrum, most aromatic protons undergo a significant upfield shift indicating aromatic interactions.[88,89] The two proton signals corresponding to the peripheral phenyl ring (H_e and H_f) represent the only exception, as these two signals show an initial minor downfield shift followed by a more significant upfield shift accompanied by broadening with MCH contents larger than 40%. This observation indicates the proximity of an electron rich group, such as O,[90] a behaviour that could be confirmed by VT-^{1}H NMR studies (Fig. S34 and S35†). These results match well with a parallel arrangement of the molecules within the stack, as most protons would thus exhibit interactions with the aromatic moieties.

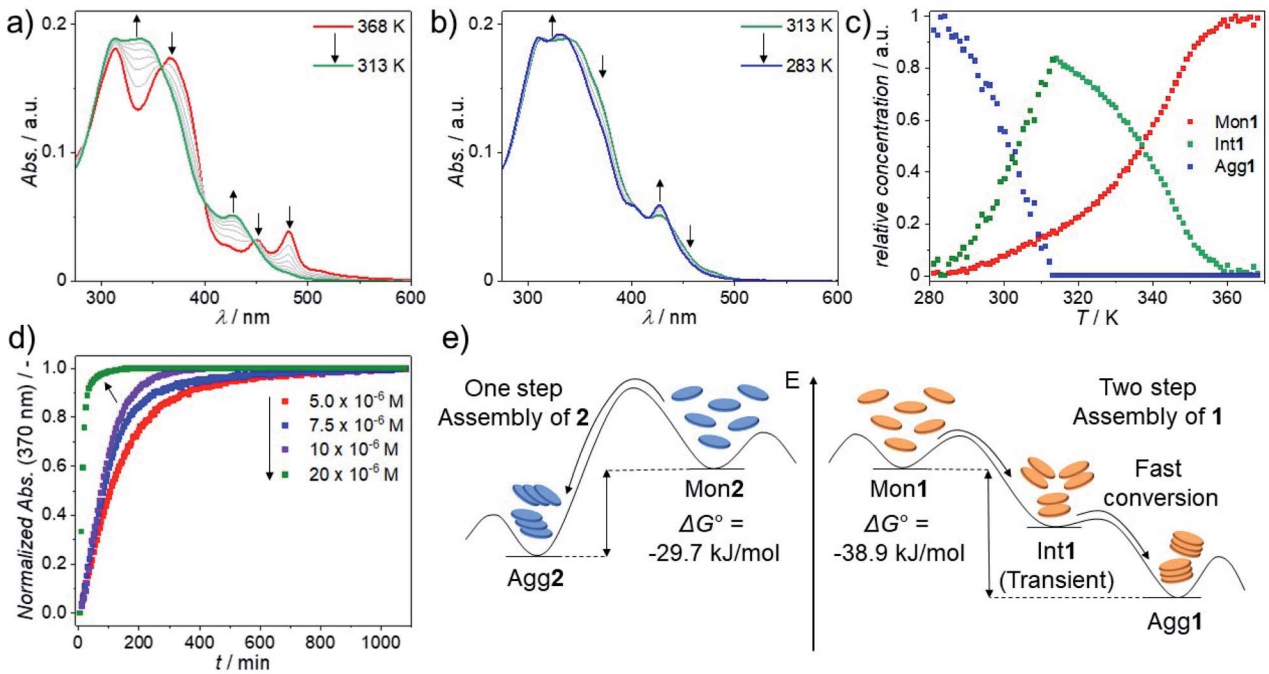

Fig. 3 VT-UV/Vis spectra of **1** between 363 K and 313 K (a) and 313 K and 283 K (b) at 3×10^{-6} M; cooling rate: 1 K min^{-1}. (c) Relative concentration of the different species involved in the aggregation process plotted *vs.* *T* estimated based on the spectral changes at $\lambda = 475$ nm and $\lambda = 370$ nm during VT-UV/Vis studies. (d) Time-dependent transformation of **Int1** to **Agg1** at different concentrations at 303 K monitored at $\lambda = 370$ nm over time after rapid temperature drop from the molecularly dissolved state at 368 K. (e) Qualitative energy landscape depicting pathway complexity for **1** and a single-step assembly behavior for **2**.

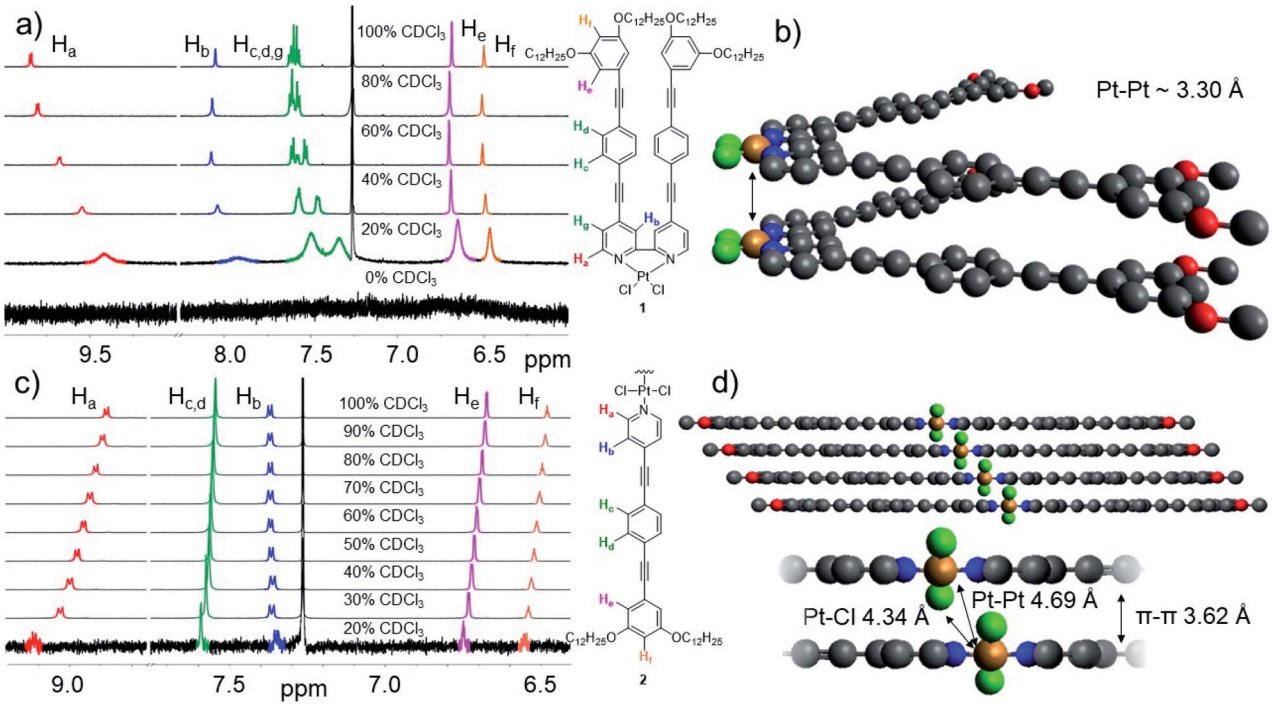

Fig. 4 (a and c) Partial solvent dependent ($CDCl_3$/MCH-d_{14}, 298 K) ^{1}H NMR spectra of **1** (a) and **2** (c) at 1×10^{-3} M. (b and d) Schematic representation of the packing modes of **Agg1** (b) and **Agg2** (d) with the most relevant intermolecular distances highlighted with arrows. The alkyl chains have been reduced to methyl groups in this representation to enhance visibility.

Additional 2D ROESY studies of **1** (Fig. S36†) also support this hypothesis. In such packing, the outer aromatic protons would come in close contact with the alkoxy oxygens of neighboring moieties, thus explaining the initial minor downfield shift observed for those signals. Such parallel stacks would enable short Pt···Pt contacts, as previously suggested by spectroscopic studies. Further, we infer from these studies that the intermediate species **Int1** represents a less ordered parallel arrangement of the aromatic moieties due to steric effects of the peripheral alkyl chains. At low temperatures, the additional planarization and decreased flexibility of the OPE backbone can facilitate a more beneficial stacking leading to better defined UV/Vis absorption bands. Unfortunately, attempts to further inspect the molecular packing of **Agg1** using XRD analysis proved unsuccessful (Fig. S37†) despite the seemingly high order within the stack. In particular, between $2\theta = 12°$ and 30°, a very broad featureless reflex is obtained, which can be rationalized by a potential flexibility of the 1D stack (*vide infra*). Based on the relatively long phosphorescence lifetimes and the emission profile of **Agg1**, we propose that the experimentally observed parallel stacking possibly results in close Pt···Pt contacts with distances shorter than <3.5 Å.

Subsequently, we also unraveled the packing mode of **Agg2**. Solvent-dependent ^{1}H NMR (Fig. 4c) in $CDCl_3$/MCH-d_{14} shows spectral changes typical for the planarization of pyridyl-based Pt(II) complexes, namely a pronounced downfield shift of the alpha proton of the pyridine moiety (8.87 ppm to 9.03 ppm) due to the increased intramolecular hydrogen bonding between the proton H_a and the Cl ligand. Additionally, the remaining protons show only negligible shifts without any signal broadening. Another interesting finding is the downfield shift of the peripheral protons H_e and H_f (Fig. 4c), which might be explained by intermolecular close contacts with electron rich groups, for example the O atoms of the neighboring molecule within the 1D stack.[90] Thus, the downfield shift suggests a relatively short-slipped J-type packing, as also indicated by UV/Vis studies and supported by XRD (Fig. S38†). Given that the proton signals remain relatively sharp during the whole experiment, the observed spectral changes should be attributed to the planarization and pre-nucleation of **2** only, which fits with the all-or-nothing aggregation behavior observed for **2** in VT-UV/Vis. In fact, if the MCH content is further increased above 60%, rapid precipitation of the large aggregates occurs, as evident from the disappearance of the NMR signals.

Combining all results for **2**, we assume the formation of initial 1D stacks with a short-slipped molecular packing, which can then agglomerate laterally *via* alkyl chain interdigitation to give larger, poorly solvated bundles of fibers.

In order to correlate the packing mode of **1** and **2** with the aggregate morphology, we employed atomic force microscopy (AFM) and scanning electron microscopy (SEM). AFM studies of **Agg1** reveal the formation of flexible fibers with a height between 1.5 and 1.8 nm (Fig. 5a, b and S40–S43†), which agrees with the molecular dimensions of **2** (length of the aromatic moiety = 1.8 nm). The values obtained from height analysis also support the interpretation of the alkoxy chains wrapping themselves around the aromatic stack. The fibers show a relatively high polydispersity with lengths as small as 50 nm up to 1

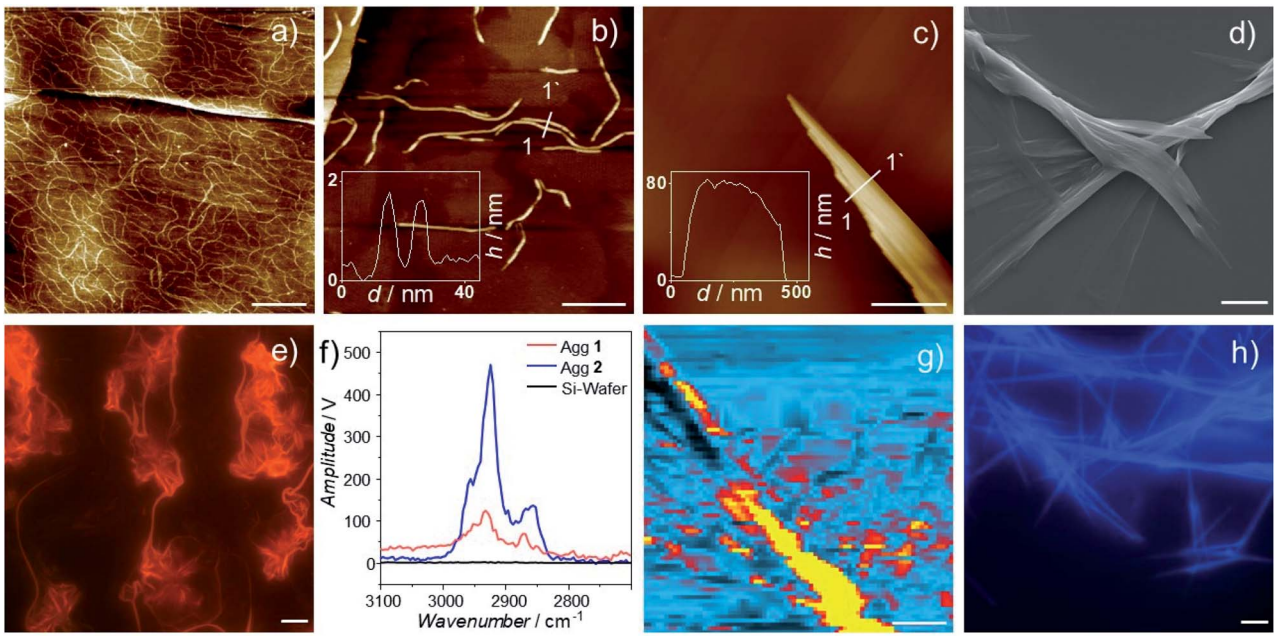

Fig. 5 AFM height images of **Agg1** (a and b) and **Agg2** (c) at 273 K on HOPG after cooling from 368 K with a cooling rate of 1 K min^{-1}. (a) $c = 5 \times 10^{-5}$ M; (b and c) $c = 2 \times 10^{-5}$ M. (d) SEM image of **Agg2**. (e and h) Luminescence micrographs of **Agg1** and **Agg2** ($\lambda_{exc} = 375$ nm). (f) AFM-IR spectra of **Agg1** and **Agg2**. (g) IR image of **Agg2** measured with $\lambda = 2925$ cm^{-1}. The scale bars correspond to 400 nm (a), 50 nm (b), 800 nm (c), 4000 nm (d), 10 μm (e), 2000 nm (g) and 10 μm (h) respectively.

μm. This observation can be rationalized by the spin-coating technique used during sample preparation which can lead to fractured aggregates, especially if thin morphologies with high aspect ratio are investigated.[48,75,91] Notably, a dense network of fibers could be observed at higher concentrations (5×10^{-5} M, Fig. 5a and S43†). The high flexibility of these structures along with the absence of high crystallinity and long-range order may be one possible explanation for the observation of a broad reflex during XRD measurements as opposed to the sharp reflexes obtained for **Agg2**. For this sample, AFM discloses the formation of large, poorly solvated bundles of stiff fibers with heights of more than 100 nm and lengths of multiple microns (Fig. 5c, S44 and S45†), as also supported by SEM (Fig. 5d and S46, S47†). The resulting structures indicate a higher long-range order compared to **Agg1**, which explains the different results obtained during XRD measurements.

Further, we attempted to microscopically correlate the morphologies observed during AFM with the luminescence properties identified in solution. To this end, we used photoluminescence microscopy and could indeed observe emissive supramolecular structures, whose emission properties matched well with previous observations (Fig. 5e and h). For solutions containing **Agg1** (5×10^{-5} M), highly flexible fibers with intense dark orange emission could be observed (Fig. 5e and S48†). In contrast, for **Agg2**, the stiff bundled fibers observed in AFM and SEM showed the typical blue fluorescence expected for metal-perturbed OPE ligands (Fig. S49†).[86,87]

Ultimately, we examined the fibers of **Agg1** and **Agg2** by AFM-IR to gain a more detailed understanding of their chemical environment (for details, see ESI†). To the best of our knowledge, this is the first time that AFM-IR is used to investigate a supramolecular polymer. Interestingly, for both polymers, two sharp IR bands that are typical for alkyl C–H stretching are observed at 2925 (ν_{anti}) and 2856 cm^{-1} (ν_{sym}) (Fig, 5f and S50, S51†).[92] These values are characteristic of interdigitation of the alkyl chains, which further supports that both polymers form an effective alkyl shell around their respective aromatic core.[92,93] This observation enabled us to create an IR image of the larger morphologies of **Agg2**, by scanning the thermal expansion attributed to the IR absorption at 2925 cm^{-1}. The resulting chemical image of **Agg2** discloses a clear match between alkyl stretching vibrations and aggregate morphology, supporting an effective shielding of the aromatic backbone by the aliphatic chains (Fig. 5g and S53†). These results further allow us to explain why both polymers exhibit identical behavior during PeakForce Tunneling AFM (Fig. S54–S57†), as the insulating alkyl shell effectively shields the central polymer backbone.[94,95]

Conclusions

In conclusion, we have unraveled the subtle interplay between coordination geometry, energy landscapes and metal–metal interactions in the context of supramolecular polymerization. For this purpose, we have designed two Pt(II) complexes that primarily differ in the molecular shape (V-shaped **1** *vs.* linear **2**) as a result of different coordination geometry (*cis* or *trans*) determined by the choice of ligand (bipyridyl *vs.* bispyridyl). Preorganized V-shaped Pt(II) complex **1** self assembles in a two-step cooperative process into 1D fibers with short metal–metal

contacts and red luminescence. In contrast, the monomer units of linear Pt(II) complex **2** are unable to establish short Pt···Pt contacts as a result of more significant steric effects than **1**, leading to a single cooperative step into microscopic bundles of fibers with short-slipped molecular arrangement and blue luminescence. Interestingly, the increase in molecular pre-organization for **1** not only enables short Pt···Pt contacts, but also promotes the emergence of pathway complexity *via* the controlled formation of an on-pathway kinetic species. These results pave the way towards functional materials based on self-assembled supramolecular polymers with potentially relevant optoelectronic applications. Work in our laboratory is underway to optimize the molecular design in order to access metallosupramolecular polymers with potential semiconductive properties arising from Pt···Pt interactions.

Conflicts of interest

There are no conflicts to declare.

Acknowledgements

N. B., K. K. K. and G. F. acknowledge the European Commission (ERC-StG-2016 SUPRACOP-715923) for funding. CAS acknowledges the DFG (EXC 1003 Cluster of Excellence "Cells in Motion"; SPP "Light Controlled Reactivity of Metal Complexes") for funding. JPP acknowledges the DFG 429646908 for funding. We thank Prof. Lambert Alff for access to XRD measurements. IM thanks the Alexander von Humboldt foundation for a post-doctoral fellowship.

Notes and references

1 S. S. Babu, V. K. Praveen and A. Ajayaghosh, *Chem. Rev.*, 2014, **114**, 1973–2129.
2 P. K. Hashim, J. Bergueiro, E. W. Meijer and T. Aida, *Prog. Polym. Sci.*, 2020, **105**, 101250.
3 M. Wehner and F. Würthner, *Nat. Rev. Chem.*, 2020, **4**, 38–53.
4 L. R. MacFarlane, H. Shaikh, J. D. Garcia-Hernandez, M. Vespa, T. Fukui and I. Manners, *Nat. Rev. Mater.*, 2021, **6**, 7–26.
5 A. S. Tayi, A. Kaeser, M. Matsumoto, T. Aida and S. I. Stupp, *Nat. Chem.*, 2015, **7**, 281–294.
6 S. Datta, Y. Kato, S. Higashiharaguchi, K. Aratsu, A. Isobe, T. Saito, D. D. Prabhu, Y. Kitamoto, M. J. Hollamby, A. J. Smith, R. Dalgliesh, N. Mahmoudi, L. Pesce, C. Perego, G. M. Pavan and S. Yagai, *Nature*, 2020, **583**, 400–405.
7 N. Sasaki, M. F. J. Mabesoone, J. Kikkawa, T. Fukui, N. Shioya, T. Shimoaka, T. Hasegawa, H. Takagi, R. Haruki, N. Shimizu, S.-I. Adachi, E. W. Meijer, M. Takeuchi and K. Sugiyasu, *Nat. Commun.*, 2020, **11**, 3578.
8 S. Ogi, T. Fukui, M. L. Jue, M. Takeuchi and K. Sugiyasu, *Angew. Chem., Int. Ed.*, 2014, **53**, 14363–14367.
9 M. Endo, T. Fukui, S. H. Jung, S. Yagai, M. Takeuchi and K. Sugiyasu, *J. Am. Chem. Soc.*, 2016, **138**, 14347–14353.
10 L. S. Shimizu, S. R. Salpage and A. A. Korous, *Acc. Chem. Res.*, 2014, **47**, 2116–2127.
11 Y. Kim, W. Li, S. Shin and M. Lee, *Acc. Chem. Res.*, 2013, **46**, 2888–2897.
12 X. Feng, B. Shen, B. Sun, J. Kim, X. Liu and M. Lee, *Angew. Chem., Int. Ed.*, 2020, **59**, 11355–11359.
13 E. E. Greciano, J. Calbo, J. Buendía, J. Cerdá, J. Aragó, E. Ortí and L. Sánchez, *J. Am. Chem. Soc.*, 2019, **141**, 7463–7472.
14 T. F. A. de Greef, M. M. J. Smulders, M. Wolffs, A. P. H. J. Schenning, R. P. Sijbesma and E. W. Meijer, *Chem. Rev.*, 2009, **109**, 5687–5754.
15 S. Ogi, N. Fukaya, D. Arifin, B. B. Skjestad, Y. Hijikata and S. Yamaguchi, *Chem.–Eur. J.*, 2019, **25**, 7303–7307.
16 F. Tantakitti, J. Boekhoven, X. Wang, R. Kazantsev, T. Yu, J. Li, E. Zhuang, R. Zandi, J. H. Ortony, C. J. Newcomb, L. C. Palmer, G. S. Shekhawat, M. Olvera de la Cruz, G. C. Schatz and S. I. Stupp, *Nat. Mater.*, 2016, **15**, 469–476.
17 A. M. Oliver, J. Gwyther, C. E. Boott, S. Davis, S. Pearce and I. Manners, *J. Am. Chem. Soc.*, 2018, **140**, 18104–18114.
18 S. Ogi, K. Matsumoto and S. Yamaguchi, *Angew. Chem., Int. Ed.*, 2018, **57**, 2339–2343.
19 N. Fukaya, S. Ogi, M. Kawashiro and S. Yamaguchi, *Chem. Commun.*, 2020, **56**, 12901–12904.
20 M. Wehner, M. I. S. Röhr, M. Bühler, V. Stepanenko, W. Wagner and F. Würthner, *J. Am. Chem. Soc.*, 2019, **141**, 6092–6107.
21 H. Ouchi, T. Kizaki, M. Yamato, X. Lin, N. Hoshi, F. Silly, T. Kajitani, T. Fukushima, K.-I. Nakayama and S. Yagai, *Chem. Sci.*, 2018, **9**, 3638–3643.
22 Y. Wang, Y. Kim and M. Lee, *Angew. Chem., Int. Ed.*, 2016, **55**, 13122–13126.
23 M. Y. Leung, S. Y. L. Leung, K. C. Yim, A. K. W. Chan, M. Ng and V. W.-W. Yam, *J. Am. Chem. Soc.*, 2019, **141**, 19466–19478.
24 A. S. Y. Law, L. C. C. Lee, M. C. L. Yeung, K. K. W. Lo and V. W.-W. Yam, *J. Am. Chem. Soc.*, 2019, **141**, 18570–18577.
25 K. K. Zhang, M. C. L. Yeung, S. Y.-L. Leung and V. W.-W. Yam, *J. Am. Chem. Soc.*, 2018, **140**, 9594–9605.
26 Z. Gao, Y. Han, Z. Gao and F. Wang, *Acc. Chem. Res.*, 2018, **51**, 2719–2729.
27 V. W.-W. Yam, V. K.-M. Au and S. Y.-L. Leung, *Chem. Rev.*, 2015, **115**, 7589–7728.
28 Q. Wan, X.-S. Xiao, W.-P. To, W. Lu, Y. Chen, K.-H. Low and C.-M. Che, *Angew. Chem., Int. Ed.*, 2018, **57**, 17189–17193.
29 K. K. Kartha, N. K. Allampally, A. T. Politi, D. D. Prabhu, H. Ouchi, R. Q. Albuquerque, S. Yagai and G. Fernández, *Chem. Sci.*, 2019, **10**, 752–760.
30 J. Chen, L. Ao, C. Wei, C. Wang and F. Wang, *Chem. Commun.*, 2019, **55**, 229–232.
31 N. Zhou, R. Hailes, Y. Zhang, Z. Chen, I. Manners and X. He, *Polym. Chem.*, 2020, **11**, 2700–2707.
32 S.-C. Chan, M. C. W. Chan, Y. Wang, C.-M. Che, K.-K. Cheung and N. Zhu, *Chem.–Eur. J.*, 2001, **7**, 4180–4190.
33 J. Ni, L.-Y. Zhang, H.-M. Wen and Z.-N. Chen, *Chem. Commun.*, 2009, 3801–3803.

34 T. J. Wadas, Q.-M. Wang, Y.-J. Kim, C. Flaschenreim, T. N. Blanton and R. Eisenberg, *J. Am. Chem. Soc.*, 2004, **126**, 16841–16849.
35 N. K. Allampally, C.-G. Daniliuc, C. A. Strassert and L. de Cola, *Inorg. Chem.*, 2015, **54**, 1588–1596.
36 C. Wang, Z. Chen, M. Liu, H. Zhong and F. Wang, *Polym. Chem.*, 2019, **10**, 3210–3216.
37 L. Herkert, A. Sampedro and G. Fernández, *CrystEngComm*, 2016, **18**, 8813–8822.
38 V. W.-W. Yam and A. S.-Y. Law, *Coord. Chem. Rev.*, 2020, **414**, 213298.
39 H. Umeyama and K. Morokuma, *J. Am. Chem. Soc.*, 1977, **99**, 1316–1332.
40 C. B. Aakeröy and K. Epa, in *Electronic Effects in Organic Chemistry*, ed. B. Kirchner, Springer Berlin Heidelberg, Berlin, Heidelberg, 2014, pp. 125–147.
41 B. Hasenkopf, J.-M. Lehn, N. Boumediene, A. Dupont-Gervais, A. Van Dorsselaer, B. O. Kneisel and D. Fenske, *J. Am. Chem. Soc.*, 1997, **119**, 10956–10962.
42 B. Hasenknopf, J.-M. Lehn, B. O. Kneisel, G. Baum and D. Fenske, *Angew. Chem., Int. Ed.*, 1996, **35**, 1838–1840.
43 J.-P. Sauvage, *Chem. Commun.*, 2005, 1507–1510.
44 J. A. Faiz, V. Heitz and J.-P. Sauvage, *Chem. Soc. Rev.*, 2009, **38**, 422–442.
45 H. Sepehrpour, W. Fu, Y. Sun and P. J. Stang, *J. Am. Chem. Soc.*, 2019, **141**, 14005–14020.
46 Y. Sun, C. Chen, J. Liu and P. J. Stang, *Chem. Soc. Rev.*, 2020, **49**, 3889–3919.
47 N. K. Allampally, M. J. Mayoral, S. Chansai, M. C. Lagunas, C. Hardacre, V. Stepanenko, R. Q. Albuquerque and G. Fernández, *Chem.–Eur. J.*, 2016, **22**, 7810–7816.
48 N. Bäumer, K. K. Kartha, N. K. Allampally, S. Yagai, R. Q. Albuquerque and G. Fernández, *Angew. Chem., Int. Ed.*, 2019, **58**, 15626–15630.
49 A. Langenstroer, K. K. Kartha, Y. Dorca, J. Droste, V. Stepanenko, R. Q. Albuquerque, M. R. Hansen, L. Sánchez and G. Fernández, *J. Am. Chem. Soc.*, 2019, **141**, 5192–5200.
50 Y. Ai, Y. Li, H. L.-K. Fu, A. K.-W. Chan and V. W.-W. Yam, *Chem.–Eur. J.*, 2019, **25**, 5251–5258.
51 A. Kobayashi, Y. Fukuzawa, H.-C. Chang and M. Kato, *Inorg. Chem.*, 2012, **51**, 7508–7519.
52 I. Stengel, C. A. Strassert, L. de Cola and P. Bäuerle, *Organometallics*, 2014, **33**, 1345–1355.
53 Y. Atoini, E. A. Prasetyanto, P. Chen, S. Silvestrini, J. Harrowfield and L. de Cola, *Chem.–Eur. J.*, 2018, **24**, 12054–12060.
54 Y. Chen, C.-M. Che and W. Lu, *Chem. Commun.*, 2015, **51**, 5371–5374.
55 W. Wu, J. Zhao, H. Guo, J. Sun, S. Ji and Z. Wang, *Chem.–Eur. J.*, 2012, **18**, 1961–1968.
56 H. Ube, Y. Yasuda, H. Sato and M. Shionoya, *Nat. Commun.*, 2017, **8**, 14296.
57 D. Cornacchia, L. Cerasino, C. Pacifico and G. Natile, *Eur. J. Inorg. Chem.*, 2008, 1822–1829.
58 Y. Han, Z. Gao, C. Wang, R. Zhong and F. Wang, *Coord. Chem. Rev.*, 2020, **414**, 213300.
59 G. V. Janjić, P. V. Petrović, D. B. Ninković and S. D. Zarić, *J. Mol. Model.*, 2011, **17**, 2083–2092.
60 P. V. Petrović, G. V. Janjić and S. D. Zarić, *Cryst. Growth Des.*, 2014, **14**, 3880–3889.
61 L. Herkert, J. Droste, K. K. Kartha, P. A. Korevaar, T. F. A. de Greef, M. R. Hansen and G. Fernández, *Angew. Chem., Int. Ed.*, 2019, **58**, 11344–11349.
62 C. Rest, M. J. Mayoral, K. Fucke, J. Schellheimer, V. Stepanenko and G. Fernández, *Angew. Chem., Int. Ed.*, 2014, **53**, 700–705.
63 Y. Chi and P.-T. Chou, *Chem. Soc. Rev.*, 2010, **39**, 638–655.
64 K. M.-C. Wong, W.-S. Tang, X.-X. Lu, N. Zhu and V. W.-W. Yam, *Inorg. Chem.*, 2005, **44**, 1492–1498.
65 W. Yang and J. Zhao, *Eur. J. Inorg. Chem.*, 2016, 5283–5299.
66 M. Milkevitch, E. Brauns and K. J. Brewer, *Inorg. Chem.*, 1996, **35**, 1737–1739.
67 J. Burgess, *Spectrochim. Acta, Part A*, 1970, **26**, 1369–1374.
68 A. Vogler and H. Kunkley, *Inorg. Chem.*, 1990, **9**, 201–220.
69 P. M. Gidney, R. D. Gillard and B. T. Heaton, *J. Chem. Soc., Dalton Trans.*, 1973, 132–134.
70 M. A. M. Meester, D. J. Stufkens and K. Vrieze, *Inorg. Chim. Acta*, 1975, **14**, 33–36.
71 M. Textor and W. Ludwig, *Helv. Chim. Acta*, 1972, **55**, 184–198.
72 V. M. Miskowski, V. H. Houlding, C.-M. Che and Y. Wang, *Inorg. Chem.*, 1993, **32**, 2518–2524.
73 R. Büchner, C. T. Cunningham, J. S. Field, R. J. Haines, D. R. McMillin and G. C. Summerton, *J. Chem. Soc., Dalton Trans.*, 1999, 711–718.
74 W. B. Connick, L. M. Henling, R. E. Marsh and H. B. Gray, *Inorg. Chem.*, 1996, **35**, 6261–6265.
75 J. Matern, K. K. Kartha, L. Sánchez and G. Fernández, *Chem. Sci.*, 2020, **11**, 6780–6788.
76 W. Lu, W.-M. Kwok, C. Ma, C. T.-L. Chan, M.-X. Zhu and C.-M. Che, *J. Am. Chem. Soc.*, 2011, **133**, 14120–14135.
77 H.-Y. Chao, W. Lu, Y. Li, M. C. W. Chan, C.-M. Che, K.-K. Cheung and N. Zhu, *J. Am. Chem. Soc.*, 2002, **124**, 14696–14706.
78 A. Bondi, *J. Phys. Chem.*, 1964, **68**, 441–451.
79 J. Sanning, L. Stegemann, P. R. Ewen, C. Schwermann, C. G. Daniliuc, D. Zhang, N. Lin, L. Duan, D. Wegner, N. L. Doltsinis and C. A. Strassert, *J. Mater. Chem. C*, 2016, **4**, 2560–2565.
80 M. Kasha, H. R. Rawls and M. Ashraf El-Bayoumi, *Pure Appl. Chem.*, 1965, **11**, 371–392.
81 M. Levitus, K. Schmieder, H. Ricks, K. D. Shimizu, U. H. F. Bunz and M. A. Garcia-Garibay, *J. Am. Chem. Soc.*, 2001, **123**, 4259–4265.
82 K. Seehafer, M. Bender and U. H. F. Bunz, *Macromolecules*, 2014, **47**, 922–927.
83 E. E. Jelley, *Nature*, 1936, **138**, 1009–1010.
84 H. M. M. ten Eikelder, A. J. Markvoort, T. F. A. de Greef and P. A. J. Hilbers, *J. Phys. Chem. B*, 2012, **116**, 5291–5301.
85 P. A. Korevaar, S. J. George, A. J. Markvoort, M. M. J. Smulders, P. A. J. Hilbers, A. P. H. J. Schenning, T. F. A. de Greef and E. W. Meijer, *Nature*, 2012, **481**, 492–496.

86 G. Das, S. Cherumukkil, A. Padmakumar, V. B. Banakar, V. K. Praveen and A. Ajayaghosh, *Angew. Chem., Int. Ed.*, 2021, DOI: 10.1002/anie.202015390.
87 E. E. Greciano, B. Matarranz and L. Sánchez, *Angew. Chem., Int. Ed.*, 2018, **57**, 4697–4701.
88 S. Lahiri, J. L. Thompson and J. S. Moore, *J. Am. Chem. Soc.*, 2000, **122**, 11315–11319.
89 C. Giessner-Prettre, B. Pullman, P. N. Borer, L. S. Kan and P. O. Ts'o, *Biopolymers*, 1976, **15**, 2277–2286.
90 X. Lu, Z. Guo, C. Sun, H. Tian and W. Zhu, *J. Phys. Chem. B*, 2011, **115**, 10871–10876.
91 A. Suzuki, K. Aratsu, S. Datta, N. Shimizu, H. Takagi, R. Haruki, S.-I. Adachi, M. Hollamby, F. Silly and S. Yagai, *J. Am. Chem. Soc.*, 2019, **141**, 13196–13202.
92 B. H. Stuart, *Infrared spectroscopy: Fundamentals and Applications*, Wiley, Chichester, 2008, p. 72.
93 G. Fernández, F. García, F. Aparicio, E. Matesanz and L. Sánchez, *Chem. Commun.*, 2009, 7155–7157.
94 K. Sugiyasu, Y. Honsho, R. M. Harrison, A. Sato, T. Yasuda, S. Seki and M. Takeuchi, *J. Am. Chem. Soc.*, 2010, **132**, 14754–14756.
95 M. Hecht, T. Schlossarek, M. Stolte, M. Lehmann and F. Würthner, *Angew. Chem., Int. Ed.*, 2019, **58**, 12979–12983.